ChemElectroChem

Research Article
doi.org/10.1002/celc.202500241

Chemistry Europe
European Chemical Societies Publishing

www.chemelectrochem.org

Controlling and Understanding the Impact of Closed Pore Size on Sodium Storage in Hard Carbons via Controlled Pyrolysis of Molecular Precursors

Ulrich Haagen, Seyedrashid Mirmasoomi, Kai Hetze, Sijia Cao, Yan Lu, Konstantin Schutjajew,* and Martin Oschatz*

Hard carbon is the most widely applied material for sodium-ion battery negative electrodes. Although capacities comparable to those of lithium/graphite can be achieved, the underlying sodium storage mechanisms remain poorly understood. From a simplified perspective, a two-step process is commonly observed: first, sodium adsorbs to the polar sites of the carbon ("sloping region") and then fills the small voids in the material ("plateau region"). In order to study the impact of the molecular size of precursors on the microstructure of carbon materials and their pore geometry, a systematic series of cyclodextrin-based hard carbons has been synthesized. It is found that the type of precursors used influences the resulting materials' pore structure, which at higher temperatures can be converted to a closed pore system. This pore conversion enables a large, low-potential sodiation plateau. Indeed, up to 75% of the total capacity is measured at potentials below 0.1 V versus Na^+/Na. Additionally, the plateau region can be extended by up to 16% by additionally considering reversible capacity below 0 V versus Na^+/Na, which means quasimetallic sodium can be stabilized within such structural motifs. Finally, gas physisorption measurements are related to charge–discharge data to identify the architecture of pores relevant to energy storage.

1. Introduction

The demand for efficient and sustainable electrochemical energy storage systems has driven extensive research into sodium-ion batteries (SIBs) as a future cost-effective alternative to lithium-ion batteries (LIBs), which were already commercialized in the 1990s.[1] Sodium is more abundant and widely available in comparison to lithium. SIBs have comparable operational voltages and largely similar chemical characteristics to LIBs, qualifying them as a drop-in technology.[2] In addition, alternative counterparts to LIB-cell components are more abundant or can be obtained from renewable sources, such as the positive electrode material, negative electrode precursors, and the current collectors.[3] Nevertheless, the development of appropriate negative electrode materials continues to represent a significant challenge. Conventional graphite electrodes, which demonstrate efficacy in LIBs, exhibit inadequate Na^+ intercalation characteristics.[4] This is due to the fact that lithium is capable of forming rather covalent bonds with graphite, resulting in a final stoichiometric composition of LiC_6 in a fully lithiated graphite electrode. Sodium, in contrast, lacks this covalent contribution and instead tends to form a rather ionic bond with carbon, rendering it practically incompatible with graphite as a negative electrode material.[5]

Consequently, the material class of hard carbons (HCs), with their characteristic turbostratically distorted and disordered graphene domains, has emerged as a promising candidate for negative electrodes in SIBs.[6] The defective graphitic microstructure results in higher interlayer distances and leads to voids between the graphene sheets. These nanometer-sized voids, also called "closed pores", are inaccessible to electrolyte solvent or gas molecules and enable the storage of quasimetallic sodium at low, constant potentials. The exact storage mechanism in HCs is still under investigation, and several models have been proposed.[7–12] In general, the typical potential profile during sodiation can be divided into two distinct regions: a sloping region at voltages above 0.1 V versus Na^+/Na and a low-voltage plateau below this threshold until the cutoff potential is reached. A widely accepted explanation, known as the "three-stage model", attributes the sloping region to the adsorption of sodium

U. Haagen, S. Mirmasoomi, Y. Lu, M. Oschatz
Institute for Technical Chemistry and Environmental Chemistry (ITUC)
Friedrich Schiller University Jena
Philosophenweg 7a, 07743 Jena, Germany
E-mail: martin.oschatz@uni-jena.de

K. Hetze, Y. Lu, K. Schutjajew, M. Oschatz
Helmholtz Institute for Polymers in Energy Applications Jena (HIPOLE Jena)
Lessingstraße 12-14, 07743 Jena, Germany
E-mail: konstantin.schutjajew@helmholtz-berlin.de

K. Hetze, S. Cao, Y. Lu, K. Schutjajew
Helmholtz-Zentrum Berlin für Materialien und Energie
Institute of Electrochemical Energy Storage
Hahn-Meitner-Platz 1, 14109 Berlin, Germany

M. Oschatz
Center for Energy and Environmental Chemistry Jena (CEEC Jena)
Friedrich-Schiller University Jena
Philosophenweg 7a, 07743 Jena, Germany

Supporting information for this article is available on the WWW under https://doi.org/10.1002/celc.202500241

ions on open surfaces and defect sites. In contrast, the low-voltage region is associated with the intercalation of Na^+ ions, followed by their clustering within the previously mentioned closed pores.[13] The plateau region reflects a more energetically favorable storage mechanism. The quasimetallic nature of the stored sodium in this region enables high capacity, high reversibility, and enhanced energy density, as the low operating voltage increases the effective working potential of the full cell.[4]

In recent years, efforts toward both increasing the energy density of HC electrodes and the understanding of the sodium storage mechanism were undertaken. For example, treatments of biomass with acids to expand interlayer spacing and induce more active sites led to a high reversible capacity of 342 mAh g^{-1} and a high initial Coulombic efficiency (ICE) of 91%.[14,15] Other treatments, such as applying coatings, helped to increase ICE and still offered a high reversible capacity of 322 mAh g^{-1}.[16] Since the closed porosity is essential for the storage of high amounts of Na^+ ions at low potentials, the nanostructure of HCs can be tuned by templating using ZnO, achieving reversible capacities of 464 mAh g^{-1} and ICE of 91.7%.[17] Nevertheless, the upscaling of HC poses a challenge, where high Coulombic efficiencies (CEs) and high energy density need to be retained throughout the transition from lab-scale to industry.[18]

Particularly, the impact of closed pore size on the sodium storage characteristics is still not sufficiently understood. In order to establish this correlation and to investigate the individual contributions of these mechanisms independently from each other, the use of model compounds with adjustable and defined properties is necessary. Ideally, a series of such model materials should differ only in closed pore size but otherwise be identical in all other parameters, such as degree of graphitization, chemical binding motifs, or particle size.[19,20] Among various biomass-derived precursors for HC synthesis, cyclodextrins (CDs)—a family of cyclic oligosaccharides composed of glucose subunits—offer these unique properties. CDs are nonreducing cyclic oligosaccharides composed of α-D-glucopyranose subunits linked by α-1,4-glycosidic bonds.[21] Structurally, CDs exhibit a truncated cone shape with a hydrophilic outer surface and a hydrophobic inner cavity.[22] This hollow, conical cavity has a depth of 7.9 Å, making CDs ideal for host–guest interactions and various functional applications.[23,24] CDs exist in three primary forms, namely α-, β-, and γ, with 6, 7, or 8 glucose subunits, resulting in cavity sizes of 5, 6, or 8 Å.[24] Their well-defined molecular structure, high oxygen content, and inherent porosity enable the formation of disordered carbon with gradually different pore sizes, facilitating Na^+ storage.

Despite this inherent potential, the impact of the different molecular sizes of α-, β-, and γ-CD on the sodium storage characteristics of the resulting HCs SIB negative electrodes has not been explored yet. So far, research has been focused on pretreatments of the precursors to tailor their structural properties, resulting in enlarged plateau capacity or improved rate capability. Ding et al. investigated a precrosslinking procedure under air atmosphere, which transformed CD-derived carbons into a 3D structure linked by carbonyl groups with enlarged closed pores leading to reversible sodium storage capacities of up to 333 mAh g^{-1} in the voltage range of 0–2.7 V versus Na^+/Na at 30 mA g^{-1}.[25] Ao et al. applied a liquid-phase molecular reconstruction strategy to create spherical HC particles with ordered pores. The resulting material had a higher surface area (129 m^2 g^{-1}) while maintaining similar plateau capacities, ICEs, and high reversible capacities of 179 mAh g^{-1} at 30 C.[26] These studies demonstrate that CDs are structurally tailorable and versatile precursors.

In this work, α-, β-, and γ-CDs were heated at 1100, 1400, and 1700 °C under inert conditions to explore the HC microstructure development during thermal treatment as a function of CD-ring size, with special focus on the evolution of the different open/closed pore environments. Since all three samples have a comparable chemical formulation, correlations between precursor molecular architecture and Na^+ storage performance can be established. As other structural parameters, like the degree of graphitization, do not differ among the carbons derived from the three CD precursors, the electrochemical properties are a direct result of the generated closed porosity. This makes it a good model material to investigate the influence of these internal voids and thus to create a link between structural and electrochemical characteristics. From α- to γ-CD, the porosity slightly increases with heat treatment, and differences in porosity can be found within the CD-series heated at 1100 °C. This open porosity, mostly smaller than 1 nm in diameter, is then closed for all samples at 1400 °C, but still detectable in small-angle X-ray scattering (SAXS). Galvanostatic charge–discharge measurements with potential limitation (GCPL) lead to reversible capacities up to 289 mAh g^{-1}, an ICE of $>$85%, and a CE of 98%. In addition, the ratio of sloping to plateau capacity is increased at higher temperatures. The sloping share is decreased from 51% at 1100 °C to 25% at 1700 °C. This work provides valuable insights into the design of high-performance biomass-derived anodes, paving the way for more efficient and sustainable sodium-ion energy storage technologies.

2. Results and Discussion

Thermogravimetric analysis under N_2 was first conducted to find a suitable precarbonization temperature of the CDs (**Figure 1**). The mass loss of CDs can be divided into two steps. From room temperature to 140 °C, a mass loss of 8.9% (α-CD), 11.9% (β-CD), and 8.2% (γ-CD) occurred, corresponding to the release of adsorbed water. The main degradation onset of the three CDs differs slightly, beginning at 310 °C for α-CD, 320 °C for β-CD, and 330 °C for γ-CD and ending at ≈420 °C. At 450 °C, the residual mass stays stable, indicating that the main liberation of hydrogen and heteroatoms in the form of volatile substances is finished. The thermogravimetric analysis (TGA) results imply that the main condensation reaction is done at 450 °C and therefore this temperature was chosen as the precarbonization temperature.

Nitrogen physisorption at −196 °C allows following the evolution of the pore structure of samples prepared at temperatures from 1100 to 1700 °C. The adsorption and desorption isotherms (**Figure 2**a) show a clear trend of increased pore volume for CDs treated at 1100 °C from α-CD-1100 to β-CD-1100 and γ-CD-1100, represented by the upward shift of the isotherm branches toward

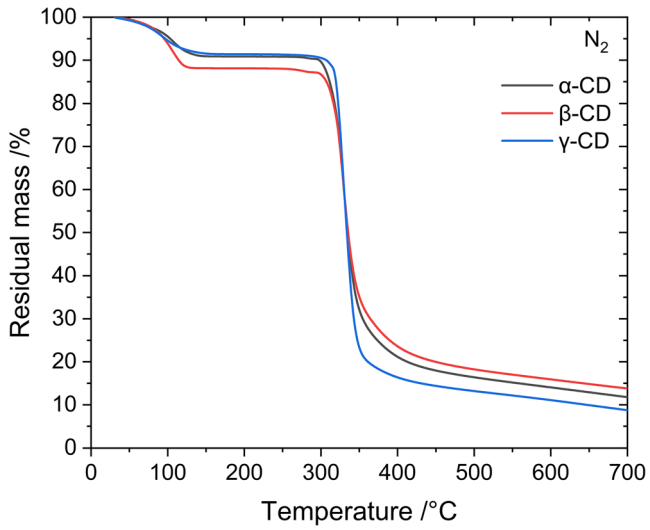

Figure 1. TGA of CDs in a temperature range of room temperature to 700 °C under nitrogen atmosphere.

higher adsorbed volumes. The shape of the three materials' isotherms is referred to as type I according to IUPAC,[27] typical of a microporous carbon material. This finding is supported by the cumulative pore volume (Figure 2b), derived from the adsorption branch, showing that the majority of pore volume is constituted by pores with sizes below 2 nm. The increased pore volume is accompanied by an enhanced specific surface area (SSA), determined by density functional theory (DFT), which ranges from 59 (α-CD-1100) to 177 $m^2 g^{-1}$ (γ-CD-1100). The shape of the isotherms of the materials obtained at 1100 °C includes a hysteresis over the entire pressure range as well as a slight increase in the nitrogen uptake during desorption, which furthermore implies that the micropores are very narrow or even partially closed. They are thus difficult to be reached by the adsorbent molecules, which leads to difficult equilibration of the measurements. A heat treatment at 1400 °C leads to the formation of a nonporous carbon, showing type II isotherms and a negligible gas uptake, which is also detectable in the cumulative pore volume curve for all three samples. The isotherms of CD-1700 also show an extremely low adsorptive uptake, although a stepwise gas uptake accompanied by a hysteresis at p/p_0 of 0.7–0.9 is observed, indicating the presence of a small volume of mesoporosity.

This observation can, however, also be due to minor contaminations arising from the aluminum-containing insulation of the high-temperature furnace, as it can be seen in the respective X-ray diffraction (XRD) patterns in Figure 4a. TGA under synthetic air (Figure S1, Supporting Information) was conducted to measure the ash content of the samples, which were 1.19% for α-CD-1700, 0.99% for β-CD-1700, and 2.98% for γ-CD-1700 (Table S1, Supporting Information). Furthermore, elemental analysis (Table S2, Supporting Information) confirmed a low contamination with carbon content of almost 100 wt% for each sample. No other analytic technique indicated an impact from it; the aluminum content is considered negligible. These findings lead to the assumption that, depending on the molecular ring size, the CD-derived carbon materials develop a distinct porosity in their microstructure at 1100 °C, which can then be transformed into closed porosity at 1400 °C. CDs-1700 do not differ much from CDs-1400 except for the additional introduced mesoporosity. The detailed sorption data is summarized in Table S3, Supporting Information.

To gain a more profound understanding, particularly regarding the micropore structure, CO_2 physisorption measurements at 0 °C were conducted (**Figure 3**a). As CO_2 molecules have a smaller kinetic diameter compared to N_2, and as the diffusion coefficient at near ambient temperature is much higher, micropores can be investigated more precisely. The corresponding isotherms follow the trend observed in N_2 physisorption. The CO_2 uptake increases for samples at 1100 °C from α to γ as a result of a higher pore volume in the microporous range. NLDFT identifies the majority of pores to lay in a pore size range between 0.3 and 0.8 nm. α-CD-1100 does show slightly larger pores (Figure 3b). CDs-1400 show a significantly decreased uptake compared to samples treated at 1100 °C, but γ-CD-1100 still shows the highest uptake. The carbon materials treated at 1700 °C are not accessible to CO_2 molecules, showing no CO_2 uptake. In addition, the micropore volume is reduced over the whole range for all samples after

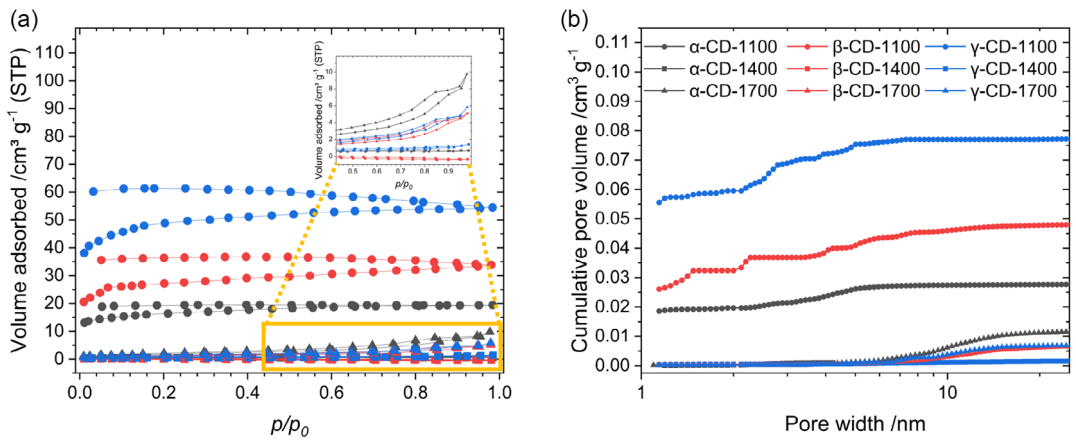

Figure 2. a) N_2 physisorption isotherms at −196 °C and b) cumulative pore volumes of CDs treated at 1100, 1400, and 1700 °C. DFT calculation was not applicable due to too low gas uptake for β-CD-1400 and is therefore omitted.

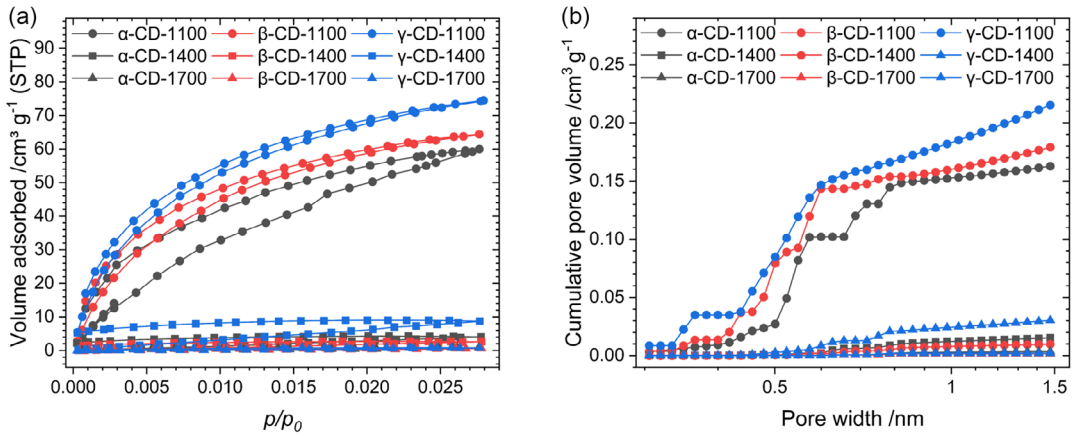

Figure 3. a) CO_2 physisorption isotherms at 0 °C and b) cumulative pore volume of CDs treated at 1100, 1400, and 1700 °C.

a heat treatment of 1400 or 1700 °C compared to 1100 °C, again confirming closure of pore entrances.

This behavior of HCs was also investigated by Dahn and coworkers in sucrose-derived HC. The "falling cards model" describes that higher temperatures reduce both the number and size of open pores, shifting the structure toward more closed, inaccessible micropores. At low carbonization temperatures, graphene sheets are loosely piled, forming many open micropores. At higher temperature, the graphitization proceeds, leading to the reorientation and compacting of graphene sheets, so that internal pores become larger in turn.[28,29] This observation is also confirmed by transmission electron microscopy (TEM) images (Figure S2, Supporting Information), which could directly prove the existence of closed pores. At a temperature of 1100 °C, indeterminate, short carbon domains manifest themselves, which show a low spread of the layers and can be described as unstructured. With higher treatment temperatures, the graphitization is clearly increased with more ordered, pronounced graphitic domains, which is in accordance with a decreasing interlayer distance and increasing I_D/I_G ratio (Table S4, Supporting Information). Furthermore, pores are still detectable throughout all temperatures.

Gas sorption analysis of the samples therefore reveals that the pore size distribution of CD-derived carbons is, on the one hand, directly inherited from the parent CD and, on the other hand, is no longer gas-accessible at temperatures higher than 1400 °C. Whether this is due to a closure of pore entrances or due to a full collapse of porosity will be discussed in the following.

As a valuable complementary technique to TEM, SAXS helped to clarify how the pore structure was influenced by the different heat treatments (Figure S3, Supporting Information). It is evident that minor variations exist among all nine samples. However, the measurements indicate that pores are discernible through the protrusion at a scattering vector q range of 0.15–0.25 $Å^{-1}$, and that their dimensions likely increase with rising temperature, as it can be estimated from the position of the shoulder and the TEM images.

To further evaluate the carbons' nanostructure, XRD was conducted on all materials. The XRD patterns (**Figure 4**a) show two typical broad reflexes of disordered carbon located at $2\theta \approx 22°–24°$ and ≈44°, referred to as (002) and (100) planes, respectively. The (002) reflex corresponds to the diffraction at the interlayer of graphene sheets. Applying the Bragg equation on the fitted XRD data with a Voigt function (Figure S4, Supporting Information) at the (002) reflex position, it is possible to estimate the distances between graphene layers (d-spacing), and a comparison of interlayer distances between all samples is shown in Table S4, Supporting Information. The decrease in the graphene interlayer distance upon heat treatment is a typical behavior for carbon materials and refers to the graphitization process, which leads to a reorganization into more ordered, graphite-like domains. The d-spacing of CDs among each other shows no significant difference and no trend. CDs-1100 show a d-spacing in the range of 3.97 and 4.10 Å, whereas the corresponding 1400 °C samples possess values of 3.98–4.02 Å. With 3.72–3.75 Å, a significant decrease in the d-spacing of samples treated at 1700 °C is observable, but with differences of 0.03 Å among the samples, the influence of this structural property is considered negligible.

As these structural evolutions are still comparable for all treated samples after high-temperature treatment (HTT), it can be stated that there is no clear influence of the number of subunits within the CD-ring on the nanostructure. However, all of the samples show a relatively high incoherent scattering background in the low-angle range, indicating scattering at rather less ordered and dimensionally larger structures in the nanometer range, often observed in porous materials. Since gas sorption analysis only revealed porosity in CD-1100 samples, it is not too far-fetched to attribute this behavior to closed porosity within the samples.

To determine whether the number of subunits in the precursor influences carbon interconnectivity and binding, Raman spectroscopy was conducted and degrees of disorder and amorphous portions of the CDs were compared. The corresponding spectra for samples after HTT are displayed in Figure 4b. There are two predominant bands to be found at wavenumbers around 1300 and 1600 cm^{-1}. The first is referred to as D-band, associated with the breathing mode of sixfold aromatic rings, typical for disordered carbon materials. This band is not observable for crystalline graphite and is only evolving with a higher degree of disorder compared to graphite. Therefore, this band can serve as a comparative measure for the bonding situation in the carbon

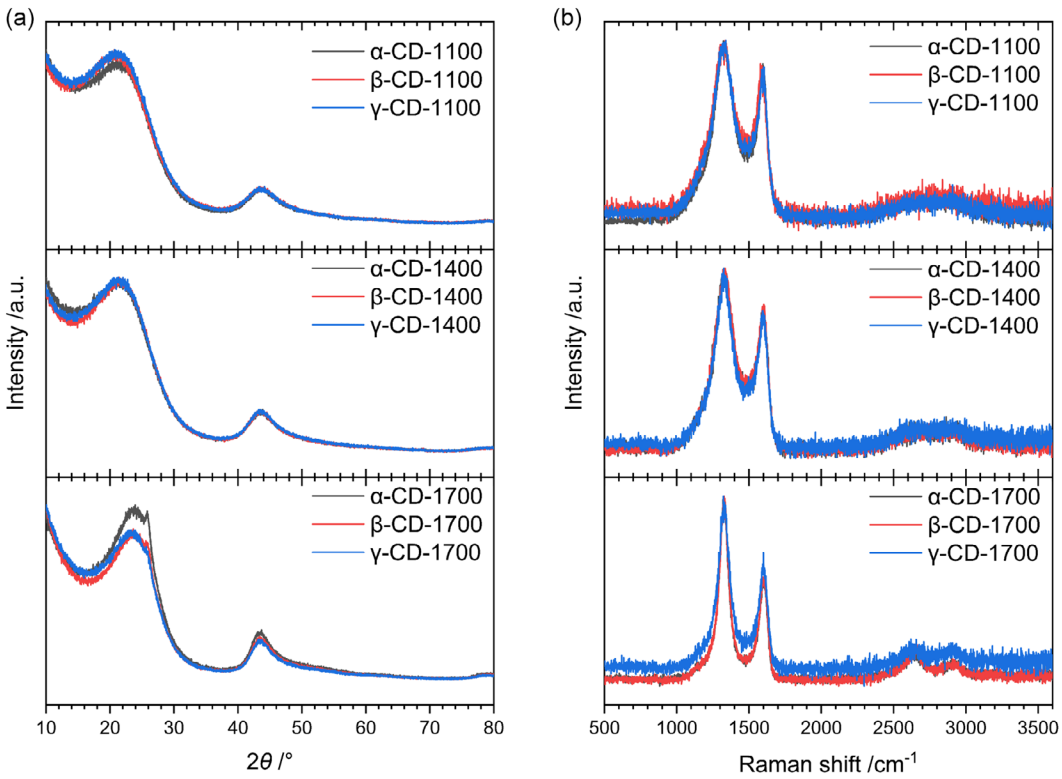

Figure 4. a) XRD patterns and b) Raman spectra of CDs treated at 1100, 1400, and 1700 °C.

framework.[30] The second band (G-band) arises from in-plane stretching of sp^2 carbon and is also found for pure graphite. The fitted Raman spectra of the samples are presented in Figure S5a–i, Supporting Information. It shows a fit of the region between 500 and 2000 cm^{-1} to a four-band model, including the *trans*-polyacetylene (TPA)-, D-, A-, and G-bands, following the method of Hu et al.[31] The TPA-band (≈1150 cm^{-1}) has been related to transpolyacetylene-like structures, typically appearing in grain boundaries or defects of carbon materials.[32] An additional sign of disorder arises from the A-band (≈1530 cm^{-1}), situated between the D- and G-bands, which can be assigned to vacancy-induced vibrations, local disorder in sp^2 carbons, or to non-six-membered rings, stemming from amorphous structures. With increasing final heat-treatment temperature, the TPA- and A-bands decrease in intensity as compared to the D- and G-bands, while the presence of D- and G-bands indicates a disordered structure dominated by sp^2 carbon, which means that the binding motif is also aromatic and cyclic in nature. Therefore, it is not surprising to find the D- and G-bands becoming more separated at higher temperatures. Furthermore, the A-band seems to vanish completely, as for better fit results, the CDs-1700 needed to be fitted to a three-band model, already indicating a higher degree of order.

A common method for the comparison of the carbon nanostructure is the calculation of the ratio of intensities of the D- and G-bands, leading to I_D/I_G. This ratio represents a measure of the ordering in the carbon framework. As carbon materials with small graphitic domains are considered herein, the growth of the D-band, and therefore a higher I_D/I_G ratio, is associated with an increase in structural order.[33] The values were calculated for all investigated samples (Table S4, Supporting Information), showing that I_D/I_G is increasing with increasing heat-treatment temperature, which could be associated with more edge defects and a more fragmented carbon nanostructure due to introduced porosity, which enables the breathing mode for more sixfold rings in the framework. Again, the I_D/I_G ratios are comparable among all CDs, showing that the carbon binding situation is not influenced by the ring size of the precursor, as it is demanded for an isolated investigation of the influence of nanoporosity on electrochemical sodium storage.

According to scanning electron microscopy (SEM) images shown in Figure S6, Supporting Information, the CDs keep their particle morphology throughout all carbonization temperatures with a particle size of a few hundred micrometers. This fact points out that the CD precursor then undergoes only local structure rearrangements. Further, it can be seen that the surface of CDs-1700 became more rough and less homogenous, which could be linked to the heat treatment at 1700 °C and the induced mesopores.

For electrochemical evaluation, all materials were characterized with GCPL experiments in sodium half cells with a current density of 20 mA g^{-1}, calculated based on total electrode mass. In the first cycle, all CD-derived materials show a notable contribution of irreversible capacity (**Figure 5**a). Solid electrolyte interphase (SEI) formation and other forms of sodium trapping are usually facilitated by open porosity and defective sites. Therefore, γ-CD-1100, with the highest porosity, has the lowest

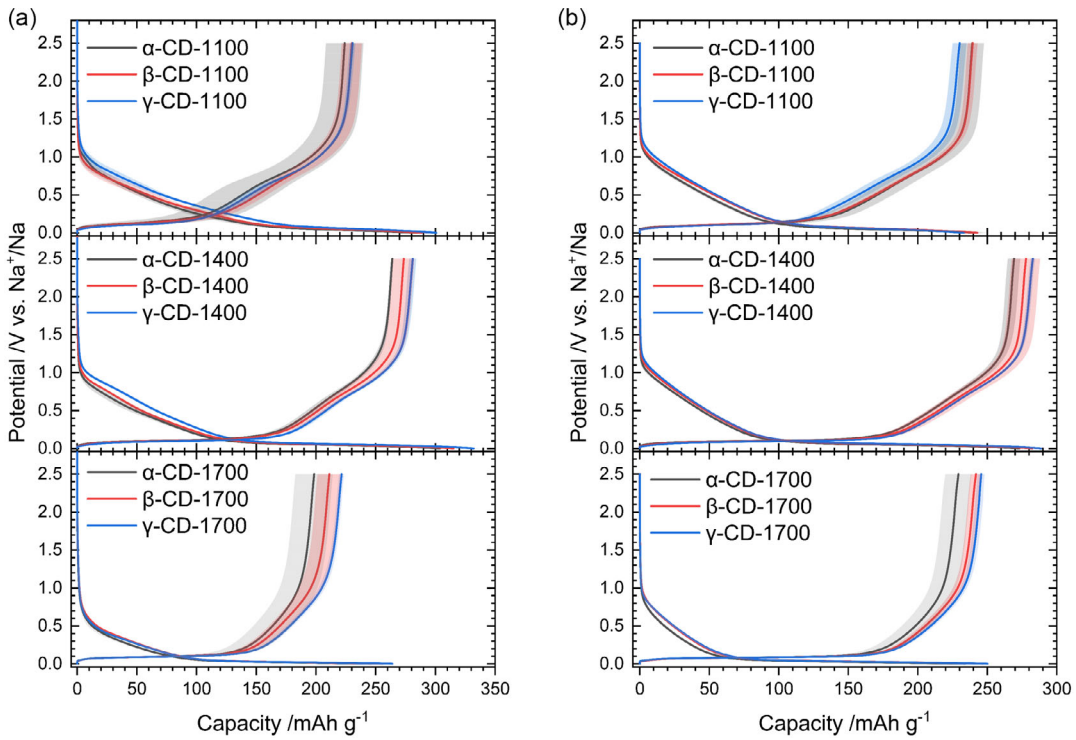

Figure 5. a) 1st cycle and b) 5th cycle of galvanostatic charge–discharge curves of CDs treated at 1100, 1400, and 1700 °C. Mean values and error bars of three repeating measurements are represented as pale-colored background.

ICE of 76.7 ± 1.0%, while α-CD-1100 and β-CD-1100, with a lower open porosity, show higher ICE of 78.6 ± 3.3% and 79.6% ± 0.7%, respectively. In contrast, the CDs-1400 with nonopen porosity show much higher ICE of 86.9 ± 0.6% (α-CD-1400), 86.8 ± 0.9% (β-CD-1400), and 84.7 ± 0.7% (γ-CD-1400). Mentionably, the ICEs of these materials are competitive with other HCs known from literature.[34]

The heat treatment at 1700 °C leads to a reduced ICE of 80.6 ± 2.3% (α-CD-1700), 82.6 ± 0.7% (β-CD-1700), and 83.9 ± 0.1% (γ-CD-1700) which could be attributed to the induced mesoporosity, whereas the CE remains nearly the same at 98% over all three temperatures and among the different CDs. After the SEI is formed, the open porosity of the materials does not play a key role in subsequent cycles anymore, since SEI-formation reactions preferentially occur at the particle surface, rendering the open pores electrolyte-inaccessible after the first cycle. Also, literature shows that initial capacity loss can originate from irreversible sodium trapping in carbon frameworks densified at higher carbonization temperatures.[35,36]

The total reversible capacity increases significantly among the samples prepared at 1100 °C, from γ-CD-1100 (233 ± 5 mAh g^{-1}) to β-CD-1100 (243 ± 3 mAh g^{-1}), and to α-CD-1100 (242 ± 9 mAh g^{-1}). In contrast, the CDs treated at 1400 °C show an increasing reversible capacity from α-CD-1400 (273 ± 5 mAh g^{-1}) to β-CD-1400 (282 ± 11 mAh g^{-1}), and to γ-CD-1400 (289 ± 2 mAh g^{-1}), which indicates that the open pore volume of the samples at 1100 °C was converted to a closed pore system at 1400 °C, enhancing the sodium storage especially of γ-CD-1400. The reversible capacity of samples treated at 1700 °C is lowered compared to 1400 °C. Due to the higher heat-treatment temperatures, the interlayer distances between the graphene layers were lowered, leading to larger pore sizes, resulting in a decreased total capacity because of the lack of stabilizing small pores. Furthermore, due to lower d-spacing, less interlayer intercalation and pseudo adsorption take place.[29]

In addition, the sloping-to-plateau ratio differs significantly when comparing all three temperature treatments. The CD-1100 samples show a quite considerable share of sloping sodiation capacity. The sloping share increases continuously with increasing pore volume, from α-CD-1100 (44.9 ± 0.3%) to β-CD-1100 (49.4 ± 1.0%), and to γ-CD-1100 (51.0 ± 0.3%) (**Figure 6**). The sloping share decreases with higher heat treatments to 37%–38% (1400 °C) and 25%–26% (1700 °C). The fact that larger CD-cycles in the carbon precursor cause slightly larger sloping capacities, which is attributed to adsorptive phenomena and solid-solution like sodium storage, and the fact that this trend occurs consistently among the samples throughout the temperature treatment process points at the chemical similarity of the carbon frameworks and closely links sloping sodium storage to (pseudo-)adsorption on defective carbon sites.[4,37]

By reducing the open pore volume, the ratio of sloping to plateau capacity was significantly reduced, which demonstrates the conversion of open pores for the samples at 1100 °C to closed pores at 1400 °C and an additional structural annealing of the carbon framework towards 1700 °C. The highest relative portion of sodium storage below 0.1 V was found for α-CD-1700 with 75.3 ± 1.0%, followed by γ-CD-1700 with 73.5 ± 0.1%, and β-CD-1700 with 73.7 ± 0.5%. The overall highest sodiation

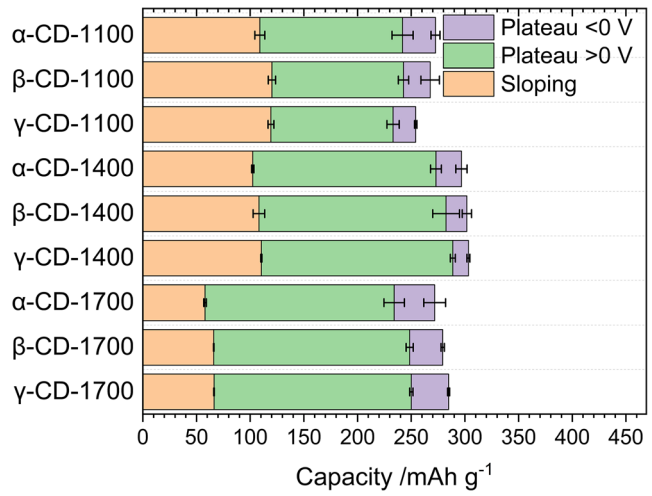

Figure 6. Bar chart comparing slope and plateau contributions to the sodiation capacity.

capacities for samples prepared at 1400 °C were the sodiation capacity of γ-CD-1400 was found to be 289 ± 2 mAh g^{-1}, which corresponds to an increase of 24%, compared to the respective 1100 °C sample. By switching from a potential-limited cycling to a capacity-limited one (Figure S7, Supporting Information), additional sodium storage capacity can be utilized.[38] The so-called quasimetallic storage mechanism continues also at voltages near or below 0 V versus Na^+/Na. We define the onset of bulk sodium plating by a small minimum peak in the sodiation curve (before a flat plateau or sharp change), indicating the heterogeneous nucleation of metallic sodium, occurring at a material-specific capacity where sodium begins to plate. The capacity before this threshold was shown to be reversible.[38]

The structural changes toward larger pores with a higher heat-treatment temperature are favorable for this mechanism, since CDs-1400 offer the lowest capacity below 0 V versus Na^+/Na with 14 ± 1 to 24 ± 5 mAh g^{-1} and in contrast, CDs-1700 samples gain the highest additional capacity of 31 ± 2 to 38 ± 10 mAh g^{-1}, if the capacity-limited method is used. Furthermore, it was shown that structural features like disorder, particle size, morphology, and interlayer distance are not influenced by the number of CD-subunits, which provides a good argument for a micropore filling mechanism at lower potentials. This finding, namely the conversion of open to closed microporosity throughout the HTT, is further supported by the existence of a direct correlation between the generated microporosity, derived from CO_2 isotherms of CDs-1100, and the relative plateau capacity (CDs-1400). Comparing physisorption and electrochemical performance of the CDs, a correlation between the pore volume of CD-1100 and the reversible capacity of CD-1400 can be established. The slightly increasing pore volume from α-CD-1100 to γ-CD-1100 becomes visible in the GCPL curves of CD-1400, showing an increased reversible capacity from α to γ. It can hence be concluded that open microporosity existing at carbonization temperatures of 1100 °C, which is rather detrimental to capacity and mostly promotes SEI-formation and irreversible reactions during the first cycle of sodiation, is transformed into closed porosity, which then serves as an anchor point for reversible sodium deposition during subsequent cycles.

Cyclic voltammetry (CV) measurements can help to clarify the origin of the increased capacity below 0 V versus Na^+/Na. In Figures S8–S10, Supporting Information, typical CV-cycles with scanning rates of 0.1, 0.2, and 0.5 mV s^{-1} of the materials are shown with a lower voltage cutoff of 0 and −0.1 V versus Na^+/Na, respectively. All CDs demonstrate comparable profiles in the initial cycle and in subsequent cycles upon Na^+ uptake and release. The initial cathodic scan reveals three primary processes. One, located between 1.7 and 0.5 V, is predominantly ascribed to the retention of Na^+ ions at defective locations and surface terminal groups. The second phenomenon, which occurs at potentials ranging from 1.0 to 0.3 V, is associated with electrolyte decomposition reactions and the formation of the SEI. The third phenomenon, which occurs at potentials lower than 0.2 V and exhibits significantly higher current densities, is assigned to the Na^+ ion storage within the carbon structure, more precisely, the closed porosity of the HC.[39]

Considering first the scan until 0 V, in all nine materials, a large capacitive contribution is found. The onset of this feature is shifted to lower potentials for materials obtained at higher pyrolysis temperatures and correlates well with the beginning of the sloping regions in the charge–discharge experiments, as it underlines the capacitive nature of the process during the potential slope. When extending the voltage window to −0.1 V, signals proving the presence of an additional process appear in both cathodic and anodic scans. In the cathodic scan, potentials falling below 0 V versus Na^+/Na lead to a continuously increasing reductive current—a characteristic signature of bulk metal plating, which is observed across various cell chemistries. During the anodic scan, the processes of sodium bulk "deplating" and reversible desodiation of HC can occasionally be resolved, as demonstrated in our previous studies.[12] However, with increasing pyrolysis temperature of the HC, this distinction becomes increasingly obscured due to the growing chemical similarity between bulk sodium and reversibly deposited ("quasimetallic") sodium. In the present case, the anodic peak appears to merge contributions from both reversible and irreversible processes.

Rate capability (RC) tests can give another important insight into the structural influence on sodium storage in disordered carbons, since the individual mechanisms responsible for sloping and plateau regions are known to respond to higher current densities differently due to specific contributions of kinetic and mass transfer limitations to the process under study. For that reason, all CD samples were assembled in two-electrode cells and measured at six different current densities between 0.05 and 0.8 Ag^{-1} (**Figure 7**). The RC test for samples treated at 1100 °C shows no clear difference at elevated current densities of 40 mA g^{-1}. At higher current densities of 80 and 200 mA g^{-1}, the more porous γ-CD-1100 retains a higher capacity of 72.7 and 43.5% versus 63.0 and 34.7% compared to the less porous material α-CD-1100 due to lower accessibility of diffusion pathways, which play a major role in the adsorptive process, especially at high current densities, and therefore affect the sloping curve.

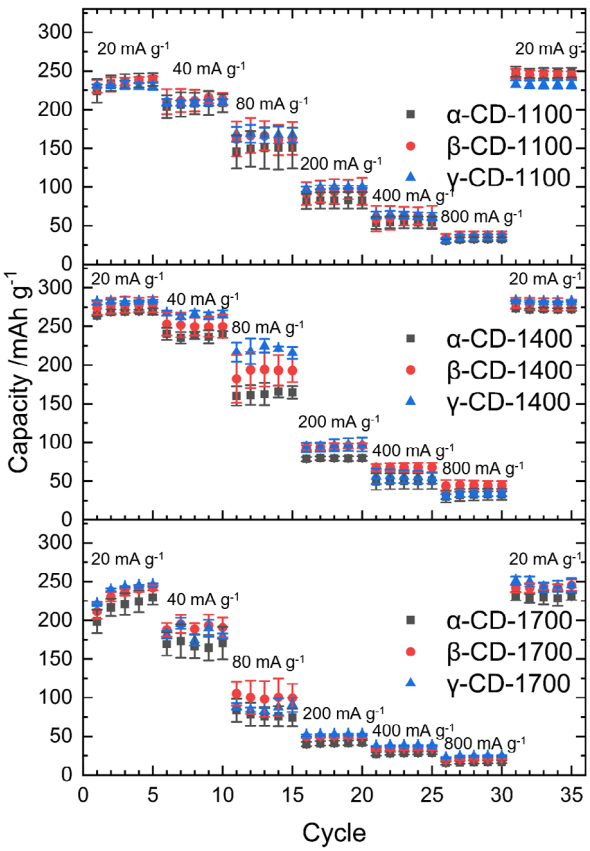

Figure 7. Rate capability tests with current densities in the range of 0.05–0.8 A g^{-1} for high-temperature treated CD samples at 1100, 1400, and 1700 °C.

This observation can be rationalized by considering the sodium-ion diffusion kinetics and transport pathways. Although closed pores enhance total capacity by storing quasimetallic sodium clusters, they are often less accessible at high charge–discharge rates due to their isolated and confined nature, which limits the rate at which sodium ions can enter and exit these sites. This phenomenon is also detectable in the charge–discharge curves in Figure S11, Supporting Information, where the sloping region is more pronounced at higher currents.

At even higher current densities, the capacities equalize again, as the adsorption occurs so quickly that the pore structure no longer has any influence. Although CDs-1400 do not exhibit open porosity, the pore structure appears to differ significantly, as the capacity increases considerably. In addition, the capacity retention was slightly enlarged up to 80 mA g^{-1} and then breaks down at 200 mA g^{-1}. In contrast, in CDs-1700, capacity retention is significantly decreased for all current densities compared to CDs treated at 1100 and 1400 °C, since the d-spacing decreases and adsorptive processes are less favorable, indicating that excessive carbonization at 1400 °C can lead to pore collapse or excessive graphitization, reducing the available ion pathways. These findings suggest that a sweet spot for heat-treatment conditions has to be met to increase the sodium storage capabilities at higher current densities.

3. Conclusion

In this study, CD as a model material was subjected to heat treatment to analyze the generated porosity and the resulting properties in electrochemical sodium storage depending on the molecular size. At similar temperatures, the samples showed no significant difference in material chemistry and crystal structure among the three different types of CDs, which could be shown with XRD and Raman measurements. In contrast, the different applied temperatures changed the carbon pore architecture.

As assumed, the structural order was increased by higher temperatures, and the interlayer distances between the graphene layers were reduced. In addition, the heat treatment changed the open porous framework at 1100 °C to a closed pore framework at 1400 °C, while the total pore volume slightly increased from α to γ, which was attributed to the closure of pore entrances. This approach thus provided a suitable model material series to investigate the influence of porosity on the electrochemical storage of sodium ions. GCPL measurements are in agreement with the Raman and XRD data in terms of the carbons showing comparable binding and stacking motifs, since no change in sodium storage behavior in voltages >0.1 V was found throughout the temperature series, which is attributed to the adsorption of sodium ions on defective sites and open porosity.

Secondly, the transformation of open to closed pores resulted in an extended low-voltage plateau from heat-treatment temperatures of 1400 °C on, supporting a micropore filling mechanism in a voltage range below 0.1 V. From CO_2 physisorption measurements, it can be concluded that pores with sizes from 0.3 to 0.8 nm are present in CDs-1100. A direct correlation of the pore volume in this range and the capacity in the low-voltage region was found, which can therefore be assigned as the main contribution to the closed pore filling mechanism. CDs-1700 were found to suffer from rather low ICE due to the formation of additional mesopores as well as lower plateau capacity and rate capability, possibly due to smaller interlayer distances in the HCs. Hence, the study is not only contributing to a deeper understanding of the sodium storage mechanism but also offers a new approach to create new model materials to further investigate the influence of open/closed pore size on electrochemical behavior.

4. Experimental Section

Synthesis of Carbon Materials

The final HCs were obtained by conducting two heat-treatment steps. First, the pristine α-CD (>98%, TCI Chemicals), β-CD (>98%, TCI Chemicals), or γ-CD (>99%, TCI Chemicals) were heated to 450 °C with 1 °C min^{-1} in a horizontal tube furnace (Nabertherm, RT/50/250/11) under a flowing N_2 atmosphere (4 L h^{-1}). In the second heating step, the material was heated to the target temperatures of 1100, 1400, and 1700 °C. The materials are denoted as α-, β-, γ-CD-X, where X refers to the final carbonization temperature. α-, β-, and γ-CD-1100/1400/

1700 were obtained by transferring α-, β-, and γ-CD-450 into a high-temperature horizontal tube furnace (HTM Reetz, LORA) and subjecting them to a further heat-treatment in flowing Ar-atmosphere (30 L h^{-1}) at 1100, 1400, or 1700 °C for 60 min with a ramp of 3.3 °C min^{-1}.

Structural Characterization

Gas physisorption measurements with N_2 and CO_2 as adsorptives were conducted using a Quantachrome Quadrasorb SI gas sorption analyzer at −196 and 0 °C, respectively. The samples were outgassed under vacuum at 150 °C for at least 12 h prior to each measurement. The multipoint brunauer-emmett-teller (BET) method in a relative pressure range of 0.05–0.3 was used to determine the SSAs. Using the adsorption branch, the pore volumes and pore size distributions were calculated by the quenched-solid DFT (QSDFT) method, assuming cylindrical and slit-like pores for N_2 at 77 K on carbon surfaces and non-local DFT (NLDFT) for CO_2 at 273 K on carbon surfaces. TGA was performed on a Netzsch STA 449 and on a Netzsch TG 309 Libra in Al_2O_3 crucibles under N_2 and synthetic air in a temperature range from 25 to 1000 °C with a heating rate of 10 °C min^{-1}. SAXS measurements were conducted using a Bruker D8 Advance equipped with a Cu K_α radiation source ($\lambda = 0.154$ nm) operating at 1600 W and a LynxEye XE-T detector operating in high-resolution mode. The experimental data were collected within the 2θ range of 0.5–5.0°, employing a step size of 0.003° with 0.5 s per step. Beam collimation was achieved by employing a primary slit with a width of 0.3 mm and 2.5° Soller slits on both the source and detector sides. Additionally, an automatic beam knife was utilized to mitigate the effects of air scattering along the beam path. XRD patterns were recorded on a Bruker D2 PHASER in Bragg-Brentano geometry in a 2θ range of 10°–80° with a resolution of 0.02° and 1 s per step with Cu K_α radiation ($\lambda = 0.154$ nm) and a Si-strip detector with 160 channels. Raman spectroscopy was measured on a "Renishaw in via" Raman microscope at a laser power of 5 mW, wavelength 633 nm, with an exposure time of 10 s for 6 accumulations. The Raman data were fitted after the four-band model using Lorentzian line shape, including the TPA-, D-, A-, and G-bands, following the method of Hu et al.[31] SEM images were taken on a TESCAN MIRA scanning electron microscope with an acceleration voltage of 1 kV. Samples were loaded on the aluminum pin-type mounts, which were covered with conductive sticky pads. Secondary and back-scattered electron detectors were applied in resolution scanning mode to record images of the sample structure. TEM was performed on a JEOL JEM-2100 (JEOL GmbH, Eching, Germany) operated at 200 kV. High-resolution TEM images were acquired at a magnification of 600 000×. For sample preparation, the materials were sonicated in ethanol for 60 min, and 5 μL of the sample dispersion was dropped onto lacey carbon-coated copper TEM grids (200 mesh, Science Services).

Electrochemical Characterization

The carbon materials were processed into electrodes through doctor blading. A total of 135 mg of the active component was mixed (mass ratio of 90:5:5) with 7.5 mg carbon black Super C65 (C-NERGY, Imerys) and 375 μL of an aqueous carboxymethylcellulose (CMC, DuPont, Walocel CRT 2000 PA) solution with a concentration of 20 mg mL^{-1}. The carbon mixture was homogenized in an impact ball mill (Pulverisette 23, Fritsch) for five minutes at a frequency of 50 Hz. The resulting ink was then applied onto a carbon-coated aluminum foil (TOB NEW ENERGY, 12–30 μm thickness) with a wet film thickness of 100 μm and an application speed of 23 mm s^{-1}. The electrodes were dried under vacuum at 70 °C for at least 12 h prior to usage. The electrodes were punched to a size of 12 mm in diameter with an area loading of 2.0–3.0 mg cm^{-2}) and placed into an argon-filled glove box, which maintained oxygen and moisture levels below 1.0 ppm. These electrodes were assembled into two-electrode PFA-Swagelok-type cells, employing the carbon materials as the working electrode. Celgard 2320 and Whatman GF/C glass fiber filters were utilized, each with a diameter of 13 mm, and saturated with 150 μL of 1M $NaPF_6$ (99.9%, Sigma Aldrich) electrolyte solution in a 6:4 v/v mixture of ethylene carbonate (Sigma Aldrich, 99%) and diethyl carbonate (Sigma Aldrich > 99%). Sodium metal (Sigma Aldrich, 99.9%) was used as both the reference and the counter electrode. GCPL experiments were executed at 20 mA g^{-1}. A voltage window of 2.5–0.002 V was applied. Unless specified otherwise, all mentioned potentials in the subsequent sections are referenced against Na^+/Na. Rate capability tests were conducted at current densities of 20, 40, 80, 200, 400, and 800 mA g^{-1} for five cycles each, before returning to the initial 20 mA g^{-1} for the last five cycles. In a final cycle, the plating capacity was determined via intentional over-sodiation at 20 mA g^{-1} with a capacity limit of 1.2 mAh. The specific capacities were calculated based on the entire electrode mass, including conductive additive and binder.

Acknowledgements

The authors thank Dr. Erik Troschke for fruitful discussions and Beate Fähndrich for measuring thermogravimetric analyses. This work was financially supported by the Research Unit ThüNaBsE – Thuringian Sodium Battery for Scalable Energy Storage (FTI Thüringen PERSONEN, 2023 FGR 0066), supported by the Free State of Thuringia and the European Social Fund Plus. A part of this work was also supported by the German Federal Ministry of Education and Research (BMBF) within project NATTER under grant number 03XP0525E and by the European Fonds for Regional Development (Europäischer Fonds für regionale Entwicklung; EFRE-Programm 2021–2027 Thüringen; Projects no. 2022 FGI 0007, DyNanoXRD and 2023 FGI 0008, SEM@CEEC).

Open Access funding enabled and organized by Projekt DEAL.

Conflict of Interest

The authors declare no conflict of interest.

Data Availability Statement

The data that support the findings of this study are openly available in [RADAR4Chem] at [https://doi.org/10.22000/9hrnmuxvrz8x396x], reference number [20250708].

Keywords: cyclodextrins · energy storage · hard carbons · sodium-ion batteries · sodium storage mechanisms

[1] A. Manthiram, *ACS Cent. Sci.* **2017**, *3*, 1063.
[2] N. Tapia-Ruiz, A. R. Armstrong, H. Alptekin, M. A. Amores, H. Au, J. Barker, R. Boston, W. R. Brant, J. M. Brittain, Y. Chen, M. Chhowalla, Y.-S. Choi, S. I. R. Costa, M. Crespo Ribadeneyra, S. A. Cussen, E. J. Cussen, W. I. F. David, A. V. Desai, S. A. M. Dickson, E. I. Eweka, J. D. Forero-Saboya, C. P. Grey, J. M. Griffin, P. Gross, X. Hua, J. T. S. Irvine, P. Johansson, M. O. Jones, M. Karlsmo, E. Kendrick, et al., *J. Phys. Energy* **2021**, *3*, 031503.

[3] P. K. Nayak, L. Yang, W. Brehm, P. Adelhelm, *Angew. Chem. Int. Ed.* **2018**, *57*, 102.
[4] D. Saurel, B. Orayech, B. Xiao, D. Carriazo, X. Li, T. Rojo, *Adv. Energy Mater.* **2018**, *8*, 1703268.
[5] O. Lenchuk, P. Adelhelm, D. Mollenhauer, *Phys. Chem. Chem. Phys.* **2019**, *21*, 19378.
[6] X. Dou, I. Hasa, D. Saurel, C. Vaalma, L. Wu, D. Buchholz, D. Bresser, S. Komaba, S. Passerini, *Mater. Today* **2019**, *23*, 87.
[7] D. A. Stevens, J. R. Dahn, *J. Electrochem. Soc.* **2001**, *148*, A803.
[8] S. Qiu, L. Xiao, M. L. Sushko, K. S. Han, Y. Shao, M. Yan, X. Liang, L. Mai, J. Feng, Y. Cao, X. Ai, H. Yang, J. Liu, *Adv. Energy Mater.* **2017**, *7*, 1700403.
[9] C. Bommier, T. W. Surta, M. Dolgos, X. Ji, *Nano Lett.* **2015**, *15*, 5888.
[10] B. Zhang, C. M. Ghimbeu, C. Laberty, C. Vix-Guterl, J.-M. Tarascon, *Adv. Energy Mater.* **2016**, *6*, 1501588.
[11] N. Sun, J. Qiu, B. Xu, *Adv. Energy Mater.* **2022**, *12*, 2200715.
[12] K. Schutjajew, J. Pampel, W. Zhang, M. Antonietti, M. Oschatz, *Small* **2021**, *17*, 2006767.
[13] Y. Morikawa, S. Nishimura, R. Hashimoto, M. Ohnuma, A. Yamada, *Adv. Energy Mater.* **2020**, *10*, 1903176.
[14] J. Wang, J. Zhao, X. He, Y. Qiao, L. Li, S.-L. Chou, *Sustain. Mater. Technol.* **2022**, *33*, e00446.
[15] Y. Wu, W. Shuang, Y. Wang, F. Chen, S. Tang, X.-L. Wu, Z. Bai, L. Yang, J. Zhang, *Electrochem. Energy Rev.* **2024**, *7*, 17.
[16] C. Yu, Y. Li, H. Ren, J. Qian, S. Wang, X. Feng, M. Liu, Y. Bai, C. Wu, *Carbon Energy* **2023**, *5*, e220.
[17] D. Igarashi, Y. Tanaka, K. Kubota, R. Tatara, H. Maejima, T. Hosaka, S. Komaba, *Adv. Energy Mater.* **2023**, *13*, 2302647.
[18] Z. Guo, K. Zheng, M. Wang, Y. Huang, Y. Zhao, H. Au, M.-M. Titirici, *Batter. Supercaps* **2025**, *8*, e202400428.
[19] S. Prykhodska, K. Schutjajew, E. Troschke, L. Kaberov, J. Eichhorn, F. H. Schacher, F. Walenszus, D. Werner, M. Oschatz, *Energy Adv.* **2024**, *3*, 1342.
[20] I. K. Ilic, K. Schutjajew, W. Zhang, M. Oschatz, *Carbon* **2022**, *186*, 55.
[21] J. Szejtli, *Chem. Rev.* **1998**, *98*, 1743.
[22] J. Szejtli, *Pure Appl. Chem.* **2004**, *76*, 1825.
[23] G. Crini, S. Fourmentin, É. Fenyvesi, G. Torri, M. Fourmentin, N. Morin-Crini, *Environ. Chem. Lett.* **2018**, *16*, 1361.
[24] B. G. Poulson, Q. A. Alsulami, A. Sharfalddin, E. F. El Agammy, F. Mouffouk, A.-H. Emwas, L. Jaremko, M. Jaremko, *Polysaccharides* **2022**, *3*, 1.
[25] H. Ding, L. Yue, Y. Liu, Y. Zhang, Q. Zhao, P. Zhi, Y. Qi, M. Xu, *New J. Chem.* **2024**, *48*, 1182.
[26] S. Ao, X. Yu, X. Wang, D. Ruan, Z. Qiao, Y. Wang, *Nano Lett.* **2025**, *25*, 1314.
[27] M. Thommes, K. Kaneko, A. V. Neimark, J. P. Olivier, F. Rodriguez-Reinoso, J. Rouquerol, K. S. W. Sing, *Pure Appl. Chem.* **2015**, *87*, 1051.
[28] J. R. Dahn, W. Xing, Y. Gao, *Carbon* **1997**, *35*, 825.
[29] E. R. Buiel, A. E. George, J. R. Dahn, *Carbon* **1999**, *37*, 1399.
[30] A. Sadezky, H. Muckenhuber, H. Grothe, R. Niessner, U. Pöschl, *Carbon* **2005**, *43*, 1731.
[31] C. Hu, S. Sedghi, A. Silvestre-Albero, G. G. Andersson, A. Sharma, P. Pendleton, F. Rodríguez-Reinoso, K. Kaneko, M. J. Biggs, *Carbon* **2015**, *85*, 147.
[32] A. C. Ferrari, J. Robertson, *Phys. Rev. B* **2001**, *63*, 121405.
[33] A. C. Ferrari, J. Robertson, *Phys. Rev. B* **2000**, *61*, 14095.
[34] M. Zhang, Y. Li, F. Wu, Y. Bai, C. Wu, *Nano Energy* **2021**, *82*, 105738.
[35] Z. Li, C. Bommier, Z. S. Chong, Z. Jian, T. W. Surta, X. Wang, Z. Xing, J. C. Neuefeind, W. F. Stickle, M. Dolgos, P. A. Greaney, X. Ji, *Adv. Energy Mater.* **2017**, *7*, 1602894.
[36] M. Carboni, J. Manzi, A. R. Armstrong, J. Billaud, S. Brutti, R. Younesi, *ChemElectroChem* **2019**, *6*, 1745.
[37] H. Alptekin, H. Au, A. C. Jensen, E. Olsson, M. Goktas, T. F. Headen, P. Adelhelm, Q. Cai, A. J. Drew, M.-M. Titirici, *ACS Appl. Energy Mater.* **2020**, *3*, 9918.
[38] K. Schutjajew, P. Giusto, E. Härk, M. Oschatz, *Carbon* **2021**, *185*, 697.
[39] H. Moon, M. Zarrabeitia, E. Frank, O. Böse, M. Enterría, D. Saurel, I. Hasa, S. Passerini, *Batter. Supercaps* **2021**, *4*, 960.

Manuscript received: June 13, 2025
Revised manuscript received: July 8, 2025
Version of record online: August 11, 2025